Signatures of Einstein-Maxwell dilaton-axion gravity from the observed jet power and the radiative efficiency

Indrani Banerjee,[1,2,*] Bhaswati Mandal,[1,†] and Soumitra SenGupta[1,‡]

[1]School of Physical Sciences, Indian Association for the Cultivation of Science, 2A & 2B Raja S. C. Mullick Road, Kolkata-700032, India

[2]Department of Physics and Astronomy, National Institute of Technology, Rourkela, Odisha-769008, India

(Received 13 July 2020; accepted 29 January 2021; published 23 February 2021)

The Einstein-Maxwell dilaton-axion gravity arises in the low energy effective action of the heterotic string theory and provides a simple framework to explore the signatures of the same. The dilaton and the axion fields inherited in the action from string compactifications have interesting consequences in inflationary cosmology and in explaining the present accelerated expansion of the Universe. It is therefore worthwhile to search for the footprints of these fields in the available astrophysical observations. Since Einstein gravity is expected to receive quantum corrections in the high curvature domain, the near horizon regime of black holes seems to be the ideal astrophysical laboratory to test these deviations from general relativity. Exact, stationary and axisymmetric black hole solution in Einstein-Maxwell dilaton-axion gravity corresponds to the Kerr-Sen spacetime that carries dilaton charge, while the angular momentum is sourced by the axion field. The ballistic jets and the peak emission of the continuum spectrum from the accretion disk are believed to be launched very close to the event horizon and hence should bear the imprints of the background spacetime. We compute the jet power and the radiative efficiency derived from the continuum spectrum in the Kerr-Sen background and compare them with the corresponding observations of microquasars. Our analysis reveals that Kerr black holes are more favored compared to Kerr-Sen black holes with dilaton charges.

DOI: 10.1103/PhysRevD.103.044046

I. INTRODUCTION

General relativity is the most competent theory of gravity, till date, due to its unprecedented success in explaining a plethora of observations [1–4] namely, the perihelion precession of mercury, the bending of light, the gravitational redshift of radiation from distant stars, to name a few. An accelerating Universe, the existence of enigmatic objects like black holes, and the detection of gravitational waves due to colliding black holes and neutron stars are some of the remarkable predictions of general relativity that increasingly received observational confirmations with the advent of advanced ground-based and space-based missions [5–9]. The recent observation of the image of the black hole M87* by the Event Horizon Telescope Collaboration has further added to its phenomenal success [10–16]. Yet, it is instructive to explore other alternate gravity models since general relativity loses its predictive power at the black hole and the big bang singularities [17–19] and the ultraviolet character of gravity continues to be ill understood. On the observational front, one needs to invoke the exotic dark matter and the dark energy [20–22] to explain the galactic rotation curves and the accelerated expansion of the Universe, respectively, if general relativity is considered to be the correct theory of gravity.

It is therefore believed that close to the Planck scale, general relativity must receive corrections from a more complete theory of gravity that also incorporates its quantum character [23–26]. A variety of alternate gravity models have therefore been put forward which can potentially fulfil the deficiencies in general relativity. This includes, higher dimensional models [27–33], higher curvature gravity, e.g., $f(R)$ [34–36] and Lanczos Lovelock models [37–40], and the scalar-tensor theories of gravity [41–45]. Many of these models are inspired from string theory [46–49], which provides a framework to unify all the known forces of nature under a single umbrella. The Einstein-Maxwell dilaton-axion (EMDA) gravity, which is central to this work is one such string inspired scalar-vector-tensor theory of gravity. Such a theory arises in the low energy effective action of superstring theories [50] when the ten-dimensional heterotic string theory is compactified on a six-dimensional torus T^6. The resultant four dimensional action comprises of $N = 4$, $d = 4$ supergravity coupled to $N = 4$ super Yang-Mills theory, in the low-energy limit. By introducing equal numbers of Kaluza-Klein and winding number modes for

*tpib@iacs.res.in
†tpbm3@iacs.res.in
‡tpssg@iacs.res.in

each cycle, this effective action can be further truncated to a pure supergravity theory exhibiting S and T dualities. The bosonic sector of this $N = 4$, $d = 4$ supergravity with a vector field is known as the EMDA gravity [51], which provides a simple framework to study classical solutions.

The EMDA theory of gravity comprises of the scalar field dilaton and the pseudoscalar axion coupled to the metric and the Maxwell field. The dilaton and the axion fields owe their origin from string compactifications and have interesting consequences in inflationary cosmology and late time acceleration of the Universe [52,53]. Various classes of black hole solutions of string inspired low-energy effective theories have been constructed [54–57] that differ significantly from the general relativistic scenario. While the static and spherically symmetric black hole solutions bear nontrivial charges associated with the dilaton and the antisymmetric tensor gauge fields, the charge neutral rotating solution in string theory is identical with the Kerr metric in general relativity [58]. However, the stationary and axisymmetric black hole solution in EMDA gravity represents the charged, rotating Kerr-Sen metric which is similar but not identical to the Kerr-Newman solution in general relativity. Although the Kerr-Sen spacetime bears strong resemblance with the Kerr-Newman background, the inherent geometry of the two black holes vary significantly. The distinguishing properties of the two spacetimes have been extensively studied [59–62] in the past. Since string theory incorporates the quantum nature of gravity and provides a promising framework for force unification, it is instructive to study the observational features of the Kerr-Sen metric, which in turn can provide an indirect testbed for string theory. Astrophysical implications of the Kerr-Sen black hole have been explored extensively [59,63–66], which includes study of null geodesics, photon motion, strong gravitational lensing, and black hole shadow. Rotation of the polarization of circularly polarized light in the vicinity of the Kerr-Sen black hole and an observation of a shadow of the same has been studied in [67].

Astrophysical systems containing black holes are known to exhibit energetic transient jets [68,69], which are often believed to be powered by the rotational energy of the black hole through the magnetic fields generated in the surrounding accreting plasma [70]. Jets are believed to be launched very close to the event horizon and consequently the related jet power encodes the information of the underlying spacetime. Similarly, the continuum spectrum emitted from the accretion disk surrounding the black holes bears the imprints of the background metric and hence can be used to extract information about the same [71]. In this work we explore the role of the Kerr-Sen background in launching jets and in affecting the continuum emission from the accretion disk. We use the radiative efficiency derived from the peak emission of the continuum spectrum and the observed jet power of microquasars as the observables. This in turn enables us to constrain the metric parameters and hence provide an indirect observational evidence of string theory.

The paper is organized as follows: in Sec. II we provide a brief overview of the EMDA gravity and the associated black hole solution. We explain the role of the background metric in affecting the radiative efficiency and the jet power in Sec. III. The theoretically computed jet power and radiative efficiency are compared with the corresponding observations of several black hole sources in Sec. IV. Finally, we conclude with a summary of our findings and discussion of our results in Sec. V.

We use $(-,+,+,+)$ as the metric convention and will work with geometrized units taking $G = c = 1$.

II. EMDA GRAVITY: AN OVERVIEW

The EMDA gravity provides a generalization of the Einstein-Maxwell action comprising of the couplings between the metric $g_{\mu\nu}$, the $U(1)$ gauge field A_μ, the dilaton field χ, and the third rank antisymmetric tensor field $\mathcal{H}_{\mu\nu\alpha}$. The resultant action up to $\mathcal{O}(\alpha')$ (where α' is the inverse string tension) in the expansion of the effective action for the heterotic string theory is given by [72]

$$\mathcal{S} = \int \sqrt{-g} d^4x \left[\frac{\mathcal{R}}{2\kappa^2} - \frac{1}{2}\partial_\nu\chi\partial^\nu\chi - 6e^{-2\sqrt{2}\kappa\chi}\mathcal{H}_{\rho\sigma\delta}\mathcal{H}^{\rho\sigma\delta} - \frac{\alpha'}{16\kappa^2} e^{-\sqrt{2}\kappa\chi}\mathcal{F}_{\alpha\beta}\mathcal{F}^{\alpha\beta} \right], \tag{1}$$

where g is the determinant and $\mathcal{R}$ the Ricci scalar with respect to the four-dimensional metric $g_{\mu\nu}$. The dilaton field is denoted by χ while $\mathcal{F}_{\mu\nu}$ represents the second rank antisymmetric Maxwell field strength tensor such that $\mathcal{F}_{\mu\nu} = \nabla_\mu A_\nu - \nabla_\nu A_\mu$, where A_μ is the $U(1)$ gauge field. In Eq. (1), the three-rank antisymmetric tensor field $\mathcal{H}_{\rho\sigma\delta}$ is defined by the relation,

$$\mathcal{H}_{\rho\sigma\delta} = \nabla_{[\delta}B_{\rho\sigma]} - \frac{\alpha'}{32\kappa\sqrt{-g}} A_{[\delta}F_{\rho\sigma]}, \tag{2}$$

where $B_{\mu\nu}$ is the second rank antisymmetric tensor gauge field also known as the Kalb-Ramond field and the square brackets associated with the indices represent the cyclic sum over the indices. The cyclic permutation of A_μ and $F_{\mu\nu}$ in Eq. (2) represents the gauge Chern-Simons term. It is important to note that the action in Eq. (1) is the low energy effective action arising in heterotic string theory taken up to $\mathcal{O}(\alpha')$ and truncated to contain only those terms which involves up to a maximum of two derivatives. Therefore, higher curvature terms in Eq. (1) and Lorentz Chern Simons terms in the definition of Eq. (2) are not taken into account in this theory [50,72]. Such a truncation holds good when we are interested in regions far away from the spacetime singularity [67,72,73]. Moreover, it leads to exact black hole solutions in string theory that we will

discuss towards the end of this section. We further mention that the effective string action also contains several gauge fields, of which only the $U(1)$ component is kept in the action, since we will be eventually interested in black hole solutions carrying $U(1)$ charge [50,72].

In four dimensions $\mathcal{H}_{\mu\nu\alpha}$ can be written in terms of the pseudoscalar field ξ, also known as the axion field [50,67,72], such that

$$\mathcal{H}_{\rho\sigma\delta} = \frac{e^{\sqrt{2}\kappa\chi}}{6\sqrt{2}}\epsilon_{\rho\sigma\delta\gamma}\partial^{\gamma}\xi - \frac{\alpha'}{32\kappa\sqrt{-g}}A_{[\rho}F_{\sigma\delta]}. \tag{3}$$

In terms of the axion field the action in Eq. (1) can be written as

$$\mathcal{S} = \int\left[\frac{\mathcal{R}}{2\kappa^2} - \frac{1}{2}\partial_{\nu}\chi\partial^{\nu}\chi - \frac{1}{2}\partial_{\nu}\xi\partial^{\nu}\xi - \frac{\alpha'}{16\kappa^2}\mathcal{F}_{\rho\sigma}\mathcal{F}^{\rho\sigma} - \frac{\alpha'}{8\kappa}\frac{6\sqrt{2}}{4!}\frac{\epsilon^{\alpha\beta\gamma\delta}}{\sqrt{-g}}\xi\mathcal{F}_{\alpha\beta}\mathcal{F}_{\gamma\delta}\right]\sqrt{-g}d^4x, \tag{4}$$

where we have considered $e^{\chi} \simeq 1$ since we are interested in regions where the classical value of the dilaton field is small, i.e., $\chi \propto \alpha'$ [72]. From Eq. (4) it is clear that the axion photon coupling constant is given by $\frac{\alpha'}{8\kappa}\frac{6\sqrt{2}}{4!}$. Further, the action in Eq. (4) also reveals that the axion and the dilaton fields are massless, which is a characteristic feature of the Lagrangian arising in heterotic string theory compactified on a six-dimensional torus [50,73,74].

The resultant Maxwell's equations coupled to the axion and the dilaton are given by

$$\nabla_{\mu}\mathcal{F}^{\mu\nu} = -\frac{\kappa}{\sqrt{2}}(\partial_{\alpha}\xi)(^{*}\mathcal{F})^{\alpha\nu}, \tag{5}$$

while equations of motion for the dilaton and the axion fields are, respectively, given by

$$\nabla_{\mu}\nabla^{\mu}\chi = -\frac{\sqrt{2}\alpha'}{16\kappa}\mathcal{F}_{\alpha\beta}\mathcal{F}^{\alpha\beta}, \tag{6}$$

$$\nabla_{\mu}\nabla^{\mu}\xi = \frac{\alpha'}{8\kappa}\frac{6\sqrt{2}}{4!}\mathcal{F}_{\gamma\sigma}(^{*}\mathcal{F})^{\gamma\sigma}, \tag{7}$$

where $(^{*}\mathcal{F})^{\mu\nu} = \frac{\epsilon^{\mu\nu\alpha\beta}}{\sqrt{-g}}\mathcal{F}_{\alpha\beta}$. The Einstein's equations assume the form

$$\mathcal{G}_{\mu\nu} = \mathcal{T}_{\mu\nu}(\mathcal{F},\chi,\xi), \tag{8}$$

where the energy-momentum tensor on the right-hand side of Eq. (8) is given by

$$\mathcal{T}_{\mu\nu}(\mathcal{F},\chi,\xi) = \frac{-2}{\sqrt{-g}}\frac{\delta\mathcal{S}(\mathcal{F},\chi,\xi)}{\delta g^{\mu\nu}}. \tag{9}$$

It turns out that the Einstein's equations with the axion, the dilaton, and the Maxwell field as the source give rise to an exact, stationary, and axisymmetric black hole solution popularly known as the Kerr-Sen solution [50] in the literature, which when expressed in Boyer-Lindquist coordinates assumes the form [75–77]

$$ds^2 = -\left(1 - \frac{2\mathcal{M}r}{\tilde{\Sigma}}\right)dt^2 + \frac{\tilde{\Sigma}}{\Delta}(dr^2 + \Delta d\theta^2) - \frac{4a\mathcal{M}r}{\tilde{\Sigma}}\sin^2\theta dt d\phi + \sin^2\theta d\phi^2\left[r(r+r_2) + a^2 + \frac{2\mathcal{M}ra^2\sin^2\theta}{\tilde{\Sigma}}\right], \tag{10}$$

where

$$\tilde{\Sigma} = r(r+r_2) + a^2\cos^2\theta, \tag{11a}$$

$$\Delta = r(r+r_2) - 2\mathcal{M}r + a^2. \tag{11b}$$

The Arnowitt-Deser-Misner (ADM) mass of the above spacetime is denoted by $M_{\mathrm{ADM}} = \mathcal{M} - \frac{r_2}{2}$ while a refers to the rotation parameter of the black hole. The dilaton parameter $r_2 = \frac{q^2}{\mathcal{M}}$ where $q = \sqrt{\frac{\alpha'}{8}}Q$ is proportional to the electric charge Q of the black hole and the square root of the inverse string tension α'. In the event q vanishes, Eq. (10) reduces to the Kerr metric. The event horizon r_H of the above spacetime is obtained by solving for $\Delta = 0$ such that

$$r_H = \mathcal{M} - \frac{r_2}{2} + \sqrt{\left(\mathcal{M} - \frac{r_2}{2}\right)^2 - a^2}. \tag{11}$$

From the form of r_2 and Eq. (11) it can be shown that $0 \le r_2 \le 2$ leads to real, positive event horizons and hence black hole solutions.

We note that the spacetime given by Eq. (10) is very similar to the Kerr-Newman solution in general relativity which differs from Eq. (10) due to the absence of the coupling of the axion and the dilaton with the Maxwell field. The solution of the axion and the dilaton fields are, respectively, given by [50,72],

$$\xi = \frac{q^2}{\sqrt{2}\kappa G\mathcal{M}}\frac{a\cos\theta}{r^2 + a^2\cos^2\theta}, \tag{12}$$

$$e^{2\chi} = \frac{r^2 + a^2\cos^2\theta}{r(r+r_2) + a^2\cos^2\theta}, \tag{13}$$

while the solution of the $U(1)$ gauge field assumes the form [50]

$$A = \frac{2\sqrt{2}qr}{\tilde{\Sigma}}(-dt + a\sin^2\theta d\phi). \tag{14}$$

We note from Eqs. (12)–(14) that all the above three fields vanish for an asymptotic observer as $r \to \infty$. Since the gravity action in Eintein gravity and EMDA gravity are identical and the additional fields present in EMDA gravity vanish asymptotically, the gravitational waves in both the theories travel with the speed of light. This is in accordance with [78,79].

It is further evident from Eqs. (12)–(14) that the coupling of the axion and the dialton to the Maxwell field is crucial, as without this, the field strengths associated with both these fields will identically vanish [Eqs. (12) and (13)]. Therefore, although the Kerr-Sen black hole carries electric charge, it essentially originates from the axion-photon coupling and not the infalling charged particles. Moreover, the presence of axionic field renders angular momentum to the black hole [Eq. (12)]. From the solution of the axion and the dilaton fields the nonzero components of $H_{\mu\nu\alpha}$ can also be evaluated [80]. When the rotation parameter in Eq. (10) vanishes (i.e., in the absence of the axionic field), the resultant spherically symmetric spacetime represents a black hole labeled by its mass, electric charge, and the asymptotic value of the dilaton field [55,81]. It is interesting to note that the Kerr-Sen background Eq. (10) can also be generated by a Newman-Janis transformation [82] of the aforesaid spherically symmetric spacetime in pure dilaton coupled gravity [55,81]. In what follows we will compute the power associated with astrophysical jets and the radiative efficiencies from the continuum spectrum, in the Kerr-Sen background. This will enable us to understand whether such a gravity theory can be instrumental in explaining these observations.

III. OBSERVATIONAL AVENUES TO TEST THE KERR-SEN SPACETIME

In this section we will consider two observational avenues to test the nature of the background spacetime, namely, the continuum spectrum emitted from the accretion disk surrounding the black hole and the power associated with the transient jets observed in such systems. Jets and accretion are ubiquitous to astrophysical systems such as active galactic nuclei and microquasars. "Transient" or "ballistic" jets consist of blobs of radio or x-ray emitting plasma moving ballistically outward with relativistic velocities. They are believed to be launched very close to the event horizon [83] and hence it is expected that the power associated with the transient jets will be affected by the nature of the background metric.

The background spacetime also affects the continuum spectrum from the accretion disk whose peak emission originates very close to the marginally stable circular orbit. The Novikov-Thorne model which is based on the "thin-disk approximation" [71] is often used to theoretically mimic the observed sectrum. This approximation holds good primarily when the black hole dwells in the high/soft state during the outbursts.

One may also explore superradiance due to scalar fields in the Kerr-Sen background. When we consider superradiant instability of a scalar field in a given background, the scalar field is treated as a perturbation to the given metric. The equation of motion of the scalar field is solved in the said background assuming an ansatz for the scalar field and the energy flux at the horizon is calculated. The flux tends to diverge below a given frequency which depends on the mass of the scalar field. The onset of superradiance causes the black hole to spin down. Therefore, if the spin of the black hole does not change over a long timescale (say, decades) then it implies that the black hole is stable to superradiance. Comparing with the available observations of black holes in the Regge plane one can therefore establish constrains on the mass of the scalar field [84–88].

It is important to note that when we consider superradiant instability of a scalar/vector field in a given background, the said field is treated as a perturbation to the given metric. However, the scalar dilaton or the pseudoscalar axion in Eq. (4) are not treated as perturbations to the metric, in fact, they are used as sources to derive the metric and hence these are charges or hairs associated with the black hole. In case one is interested in investigating superradiant instability of scalar/vector bosons in the Kerr-Sen background, then one needs to introduce test fields as perturbation to the Kerr-Sen background. This has been addressed with a test scalar field in [89] and for a massive vector field in [90].

In the next section we will discuss how the continuum spectrum and the power associated with transient jets can be used to probe the background metric. A similar analysis has been performed earlier [91] in the context of Johannsen-Psaltis spacetime.

A. Radiative efficiency of black holes from the continuum spectrum

In this section we highlight the basic features of the Novikov-Thorne model [71] which is used to describe the continuum spectrum observed in the black holes. According to this model the electromagnetic emission from the accretion disk surrounding the black hole chiefly contributes to the continuum spectrum. The accretion disk is assumed to be geometrically thin such that matter is accreted chiefly along the equatorial plane. The accreting particles are assumed to maintain nearly circular orbits along the geodesics, with negligible radial velocity arising due to viscous stresses, which facilitates the inspiral and fall of matter into the black hole. Since the accreting particles follow nearly circular geodesics the gravitational pull of the central black hole supercedes the forces due to radial pressure gradients. This in turn implies that the

specific internal energy of the accreting fluid can be neglected compared to its rest energy such that special relativistic corrections to the local hydrodynamic, thermodynamic, and radiative properties of the fluid can be safely ignored compared to the general relativistic effects due to the presence of the black hole.

As the matter falls towards the black hole they lose gravitational potential energy, which gets converted into electromagnetic radiation interacting very effectively with the accreting matter before being radiated out of the system. Consequently, the geometrically thin accretion disk is also optically thick and practically no heat is trapped with the accretion flow. Due to the efficient interaction between matter and radiation, every annulus of the disk emits a black body commensurate with the temperature of the disk. The total emission from the accretion disk is therefore a multicolor black body spectrum peaking in soft x-rays for stellar mass black holes. For a more detailed description of the thin-disk model one is referred to [71,92,93]. This model provides an accurate description of the observed continuum spectrum when the black hole is in the high/soft state during the outbursts. In such a scenario the peak emission from the accretion disk generally emerges from the marginally stable circular orbit. The peak temperature and flux of this continuum spectrum are used to estimate the radius of the innermost stable circular orbit $r_{\rm isco}$ of a black hole, provided its mass, distance, and inclination angle are known from independent measurements. The radius of the innermost stable circular orbit in turn depends on the background metric and is obtained from the effective potential $V_{\rm eff}$ in which the accreting particles move. The effective potential in a stationary and axisymmetric spacetime is given by [71,92,93],

$$V_{\rm eff}(r) = \frac{E^2 g_{\phi\phi} + 2EL g_{t\phi} + L^2 g_{tt}}{g_{t\phi}^2 - g_{tt} g_{\phi\phi}} - 1, \tag{15}$$

where, g_{tt}, $g_{t\phi}$, and $g_{\phi\phi}$ are the metric elements given in Eq. (10) while E and L are the specific energy and specific angular momentum of the particles such that

$$E = \frac{-g_{tt} - \Omega g_{t\phi}}{\sqrt{-g_{tt} - 2\Omega g_{t\phi} - \Omega^2 g_{\phi\phi}}}, \tag{16}$$

and

$$L = \frac{\Omega g_{\phi\phi} + g_{t\phi}}{\sqrt{-g_{tt} - 2\Omega g_{t\phi} - \Omega^2 g_{\phi\phi}}}, \tag{17}$$

where the angular velocity $\Omega = (d\phi/dt)$ of the test particles is given by

$$\Omega = \frac{d\phi}{dt} = \frac{-g_{t\phi,r} \pm \sqrt{\{-g_{t\phi,r}\}^2 - \{g_{\phi\phi,r}\}\{g_{tt,r}\}}}{g_{\phi\phi,r}}. \tag{18}$$

The radius of the innermost stable circular orbit corresponds to the inflection point of this effective potential such that $V_{\rm eff} = \partial_r V_{\rm eff} = 0 = \partial_r^2 V_{\rm eff}$ [93]. Therefore, a measurement of $r_{\rm isco}$ from the continuum spectrum can be used to constrain the background spacetime. In particular, if the background is taken to be Kerr spacetime, then a measurement of $r_{\rm isco}$ from the continuum spectrum can be used to predict the angular momentum of the black holes [94]. This forms the basis of the continuum fitting method used to determine the black hole spins [95].

The continuum fitting method eventually determines the radiative efficiency η of a black hole which corresponds to the gravitational binding energy of a test particle at the innermost stable circular orbit, such that

$$\eta = 1 - E_{\rm isco} \tag{19}$$

where $E_{\rm isco}$ is the specific energy of the test particle computed at $r_{\rm isco}$. It is evident from Eq. (19) that η also depends on the background metric and if the spin of the black hole is determined by the continuum fitting method then η can also be evaluated.

In the event we consider departure from general relativity, the radiative efficiency computed from the continuum emission by the above method can be used to determine the allowed values of the metric parameters for a given black hole. Figure 1(a) depicts the variation of the radiative efficiency η [Eq. (19)] with the dimensionless spin parameter a for various values of the dilaton parameter r_2 (here and in the rest of the paper the spin and the dilaton parameter are scaled by the mass of the black hole, i.e., $r_2 \equiv r_2/\mathcal{M}$ and $a \equiv a/\mathcal{M}$.) We note that for a given r_2, η increases with a.

B. Jets in astrophysical systems and the Blandford-Znajeck model

Microquasars generally exhibit two different types of jets [69]: (i) steady, nonrelativistic jets (also known as outflows) which are common during the hard state [96] and are observed at a wide range of accretion luminosities and (ii) transient or ballistic jets that occur at the Eddington luminosity during state transitions, mainly when the source transits from the hard to the soft state at high accretion rates. Transient jets which reach out to parsec scales are relativistic in nature and are believed to be launched very close to the event horizon [83]. Hence these jets are often instrumental in extracting large fractions of the spin energy of the black holes [97]. Since the main goal of this work is to constrain the Kerr-Sen metric from the jet power, we will be concentrating on the relativistic transient jets in this work.

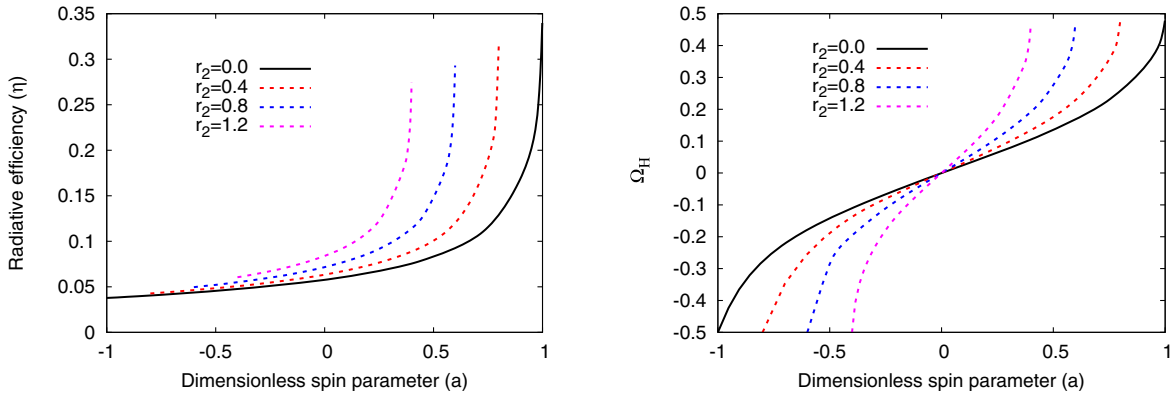

FIG. 1. This figure illustrates the variation of (a) the radiative efficiency η and (b) the angular velocity of the horizon Ω_H with the dimensionless spin parameter a for various choices of the dilaton parameter r_2. The black solid line corresponds to the Kerr scenario.

The exact mechanism of generating the transient jets is unknown, although a number of theoretical models [98–100] have been proposed that can potentially explain the observed jet power. One of the popular models used for explaining the formation of relativistic jets was put forward by Blandford and Znajeck [70] where the relativistic jets are powered by extracting the rotational energy of the black holes by means of magnetic field lines which are supported by the surrounding accretion disk due to the presence of electric currents. The Blandford-Znajeck model was originally proposed for Kerr black holes surrounded by a stationary, axisymmetric force-free magnetosphere. However, this can be generalized to any stationary, axisymmetric spacetime.

The force-free magnetosphere has the property that the particle inertia is negligible such that the total energy momentum tensor is dominated by the energy-momentum tensor due to the electromagnetic fields, i.e.,

$$T^{\rm tot}_{\mu\nu} \approx T^{\rm EM}_{\mu\nu} = F_{\mu\rho}F^{\rho}_{\nu} - \frac{1}{4}g_{\mu\nu}F^{\alpha\beta}F_{\alpha\beta}, \tag{20}$$

which satisfies the conservation equation,

$$\nabla^{\mu}T^{\rm EM}_{\mu\nu} = 0. \tag{21}$$

In Eq. (21), $F_{\mu\nu} = \partial_\mu A_\nu - \partial_\nu A_\mu$ is the Faraday tensor and A_μ is the gauge field. In a force-free magnetosphere it can be shown that

$$\frac{A_{t,r}}{A_{\phi,r}} = \frac{A_{t,\theta}}{A_{\phi,\theta}} = -\omega(r,\theta), \tag{22}$$

where $\omega(r,\theta)$ represents the electromagnetic angular velocity [70]. With this force-free condition [Eq. (22)] and assuming A_μ is axisymmetric and time independent, one can write the Faraday tensor in the form

$$F_{\mu\nu} = \sqrt{-g}\begin{pmatrix} 0 & -\omega B^{\theta} & \omega B^{r} & 0 \\ \omega B^{\theta} & 0 & B^{\phi} & -B^{\theta} \\ -\omega B^{r} & -B^{\phi} & 0 & B^{r} \\ 0 & B^{\theta} & -B^{r} & 0 \end{pmatrix}. \tag{23}$$

It can be shown that the power associated with the relativistic jet in the context of the Blandford-Znajeck model is given by (Appendices A and B)

$$P_{\rm BZ} = 4\pi \int_0^{\pi/2} \sqrt{-g}T^{r}_{t}d\theta, \tag{24}$$

where, T^{r}_{t} represents the radial component of the Poynting flux evaluated at the jet launching radius, which happens to be the event horizon. This is given by

$$T^{r}_{t} = 2r_H M \sin^2\theta (B^r)^2 \omega[\Omega_H - \omega]|_{r=r_H}, \tag{25}$$

where r_H and $\Omega_H = a/(2Mr_H)$ are the horizon radius and the angular velocity of the event horizon, respectively.

At this stage, it is impossible to calculate the power $P_{\rm BZ}$ associated with the jet without knowing the form of ω and B^r. Ideally this should be obtained by solving Eq. (21), which is quite nontrivial. Therefore, we follow the standard approach [101,102], where an exact solution of Eq. (21) is obtained for the Schwarzschild spacetime and then an expansion in Ω_H is considered to find the rotating solution perturbatively. With this expansion, the jet power in the Blandford-Znajeck model at the leading order in Ω_H is given by

$$P_{\rm BZ} = k\Phi^2_{\rm tot}\Omega^2_H, \tag{26}$$

where $k = 1/6\pi$ for a split monopole field profile and $k = 0.044$ for a paraboloidal profile. In Eq. (26), $\Phi_{\rm tot}$ denotes the magnetic flux threading the event horizon and is given by

$$\Phi_{\rm tot} = 2\pi \int_0^{\pi} \sqrt{-g}|B^r| d\theta. \tag{27}$$

For a more detailed derivation of the jet power in the Blandford-Znajeck model assuming Kerr-Sen background, one is referred to Appendices A and B. We note that the dependence of $P_{\rm BZ}$ on the metric arises through Ω_H. In Fig. 1(b) we plot the variation of Ω_H with the dimensionless spin parameter a for various values of r_2. The figure shows that, for a given r_2, $|\Omega_H|$ increases with $|a|$.

IV. COMPARISON OF THE THEORETICAL MODEL WITH OBSERVATIONS

We have noted in Sec. III that the radiative efficiency [Eq. (19)] and the jet power [Eq. (26)] are both sensitive to the background metric. Therefore, if these quantities are observationally constrained for some of the black holes, it can be used to gain some insight on the observationally favored magnitude of the dilaton parameter r_2. Our observational sample comprises of six x-ray binaries, namely, GRS1915 + 105, GROJ1655-40, XTEJ1550-564, A0620-00, H1743-322, and GRS1124-683 whose jet power and radiative efficiency are known from observations [97,103,104].

The spins of these microquasars have been estimated by the continuum fitting method which in turn have been used to evaluate the radiative efficiencies of these black hole sources. The mass M, the distance D, the inclination angle i, the dimensionless spin (Kerr parameter) a, and the radiative efficiency η of these black holes are reported in Table I [103].

For the six microquasars, we follow the prescription of [97,104] to determine the observed jet power that assumes that the entire power in the transient jet is proportional to the peak 5 GHz radio flux density $(S_{\nu,0})_{\rm max,\,5\ GHz}$, also reported in Table I. This observed flux density needs to be appropriately Doppler boosted for both the approaching and the receding jets and summed to obtain the corresponding emitted flux density [83,104]. This is scaled by the distance of the black hole to obtain the luminosity and by the black hole mass to remove any dependence. Using the natural units for these systems the proxy for the jet power is given by [97,104]

$$P_{\rm jet} = \left(\frac{\nu}{5\ {\rm GHz}}\right)\left(\frac{S^{\rm tot}_{\nu,0}}{\rm Jy}\right)\left(\frac{D}{\rm kpc}\right)^2\left(\frac{M}{M_\odot}\right)^{-1} \tag{28}$$

where, $\nu S^{\rm tot}_{\nu,0}$ is the beaming corrected maximum flux after taking into account the approaching and receding jets [83,104]. In order to correct for the beaming the Lorentz factor Γ associated with the jet is taken to be $2 \lesssim \Gamma \lesssim 5$ [105,106], commensurate with the mildly relativistic jets in microquasars.

Assuming the Lorentz factors of $\Gamma = 2$ and $\Gamma = 5$ and using Eq. (28), the Doppler corrected jet powers for the six black hole sources are reported in Table II [103,107], which are used for comparison with the theoretically derived jet power given by Eq. (26). We note that, in Eq. (26), the dependence of the jet power on the metric comes through the term Ω_H^2, while the remaining terms depend on the nature and properties of the magnetic field threading the event horizon. We rewrite Eq. (26) in the form

$$\log P = \log K + 2 \log \Omega_H, \tag{29}$$

where the magnitude of K has been estimated [97,107] by fitting Eq. (29) to the observed jet power plotted against Ω_H, which in turn is calculated from the spin estimated by the continuum fitting method (Sec. III B). Since the jet power depends on the Lorentz factor Γ, the magnitude of K varies accordingly. It turns out that, for $\Gamma = 2$ and $\Gamma = 5$, $\log K = 2.94 \pm 0.22$ and $\log K = 4.19 \pm 0.22$, respectively, at 90% confidence level [107]. In what follows we continue to use these values of K while constraining the metric parameters r_2 and a from the observed jet power, as K is independent of the background spacetime.

A. Results

1. A0620-00: the x-ray binary A0620-00 comprises of a K-type main sequence star and a black hole of 6.6 $M_\odot$ [108]. It is the nearest known x-ray binary to the solar system [109] and has an orbital period of 7.75 hours [110,111]. The distance and inclination of the source are reported in Table I [108]. The spin of the source has been determined by the continuum fitting method with $-0.59 < a < 0.49$, the best-fitting value being $a = 0.12 \pm 0.19$ [111], which

TABLE I. Parameters of the transient black hole binaries.

BH Source	$M(M_\odot)$	D(kpc)	i°	a	η	$(S_{\nu,0})_{\rm max,\ 5\ GHz}$(Jy)
A0620-00	6.61 ± 0.25	1.06 ± 0.12	51.0 ± 0.9	0.12 ± 0.19	$0.061^{+0.009}_{-0.007}$	0.203
H1743-322	8.0	8.5 ± 0.8	75.0 ± 3.0	0.2 ± 0.3	$0.065^{+0.017}_{-0.011}$	0.0346
XTEJ1550-564	9.10 ± 0.61	4.38 ± 0.5	74.7 ± 3.8	0.34 ± 0.24	$0.072^{+0.017}_{-0.011}$	0.265
GRS1124-683	$11.0^{+2.1}_{-1.4}$	$4.95^{+0.69}_{-0.65}$	$43.2^{+2.1}_{-2.7}$	$0.63^{+0.16}_{-0.19}$	$0.095^{+0.025}_{-0.017}$	0.45
GROJ1655-40	6.30 ± 0.27	3.2 ± 0.5	70.2 ± 1.9	0.7 ± 0.1	$0.104^{+0.018}_{-0.013}$	2.42
GRS1915 + 1051	$12.4^{+1.7}_{-1.9}$	$8.6^{+2.0}_{-1.6}$	60.0 ± 5.0	0.975 $a_* > 0.95$	$0.224\ \eta > 0.19$	0.912

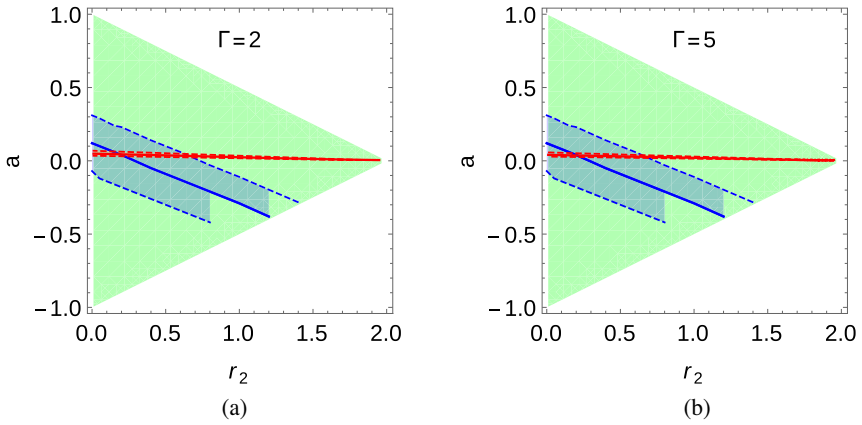

FIG. 2. Black hole source A0620-00. The orange shaded area denotes the values of r_2 and a when the theoretical jet power $P_{\rm BZ}$ equals the observed luminosity Doppler boosted by the Lorentz factor with (a) $\Gamma = 2$ and (b) $\Gamma = 5$. The solid red line corresponds to the contour in the r_2-a plane when $P_{\rm BZ}$ equals $P_{\rm jet}$ (Table II), while the dashed red lines denote the error bar of 0.3 dex about $P_{\rm jet}$. The blue shaded region in the figure denote the values of r_2 and a when the observed η is reproduced by the theoretically calculated radiative efficiency. The blue solid line corresponds to the central value of the observed η while the blue dashed lines represent the associated error bars (Table I). The green shaded region indicates the values of r_2 and a giving rise to a real positive event horizon and hence a black hole solution. For more discussion see text.

in turn enables us to compute its radiative efficiency η (Table I). The blue shaded region in Fig. 2 represents the allowed values of r_2 and a, which can explain the radiative efficiency of this source within the error bars. The blue solid line corresponds to the contour in the r_2-a plane when the theoretical radiative efficiency given by Eq. (19) coincides with the central value of the observed η (Table I). The blue dotted lines are similarly associated with the error bars in the observed η.

Radio observations of the object reveal the presence of strong radio jets [111,112], the 5 GHz radio flux density being 0.203 Jy [97] (Table I). As discussed earlier, the observed radio flux density is converted to the emitted radio luminosity by Doppler deboosting with Lorentz factors $\Gamma = 2$ and $\Gamma = 5$, the putative values being reported in Table II. These are then compared with the theoretical jet power $P_{\rm BZ}$ [given by Eq. (27)] to discern the allowed values of r_2 and a from jet related observations. An error of 0.3 *dex* is considered in the observed jet power $P_{\rm jet}$ [97,107]. The orange shaded region in Fig. 2 depicts the allowed values of r_2 and a that can explain the observed jet power within the error bars. Again the solid red line depicts the contour in the r_2-a plane, which can reproduce the central value of $P_{\rm jet}$ while the dashed red lines represent the values of r_2 and a that can explain the jet power with error of 0.3 *dex* about the central value.

The results for $\Gamma = 2$ and $\Gamma = 5$ are depicted in Figs. 2(a) and 2(b), respectively. The green shaded region denotes the parameter space in the r_2-a plane with real positive event horizons, which leads to black hole solutions in EMDA gravity. In the subsequent discussion, the definition of the blue, orange and the green shaded region remains the same for the remaining x-ray binaries. From Fig. 2 we note that the observed η cannot be explained if $r_2 > 1.5$. The jet power on the other hand can be reproduced by almost the entire range of r_2 although the Kerr parameter varies between $0 \lesssim a \lesssim 0.05$. The intersection of the blue and the orange shaded region represents the allowed values of r_2 and a such that both the observations related to $P_{\rm jet}$ and η can be explained. From Fig. 2 we note that $0 \lesssim r_2 \lesssim 0.8$ can describe both the aforesaid observations. Moreover, the allowed ranges of spin from both the observations exhibit an overlap in the general relativistic scenario ($r_2 = 0$).

2. H1743-322: this galactic microquasar is located at a distance of 8.5 ± 0.8 kpc and has an inclination of $75 \pm 3°$ [113]. Although the mass of this object has not been dynamically measured it has been predicted to be in the range 8–13 $M_\odot$ [103,114]. The companion star consists of a late-type main sequence star located in the galactic bulge [115] and the orbital

TABLE II. Proxy jet power values in units of $\rm kpc^2 GHz Jy M_\odot^{-1}$.

BH Source	$P_{\rm jet}\|_{\Gamma=2}$	$P_{\rm jet}\|_{\Gamma=5}$
A0620-00	0.13	1.6
H1743-322	7.0	140
XTEJ1550-564	11	180
GRS1124-683	3.9	390
GROJ1655-40	70	1600
GRS1915 + 105	42	660

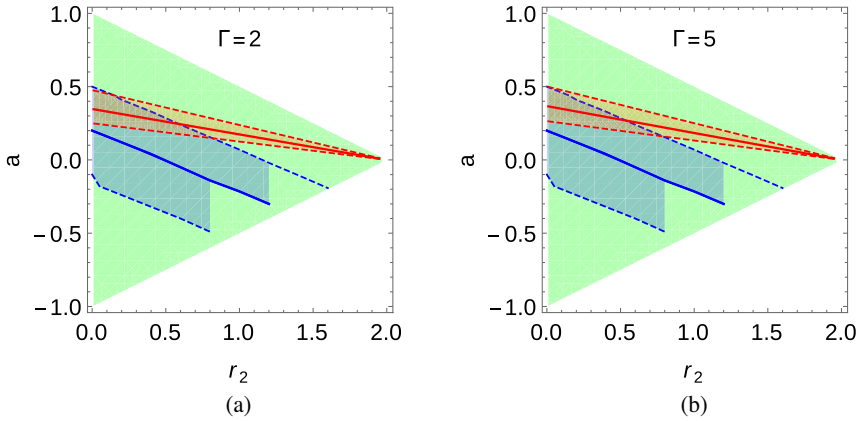

FIG. 3. Black hole source H1743-322. The orange shaded region in the figure denote the values of r_2 and a that can reproduce the observed $P_{\rm jet}$ with (a) $\Gamma = 2$ and (b) $\Gamma = 5$, within the error bars. The blue shaded region is associated with the allowed values of r_2 and a that can address the observed η (Table I) within the error bars. For more discussion see text.

period of the binary is ten hours [116]. The spin of the object estimated by the continuum fitting method turns out to be 0.2 ± 0.3 at 68% confidence and $-0.3 < a < 0.7$ at 90% confidence [113]. The corresponding radiative efficiency is reported in Table I. As before, the blue shaded region in Fig. 3 is associated with the allowed values of r_2 and a that can describe the observed radiative efficiency within the error bars. The blue lines denote the contours in the r_2-a plane when the observed eta is reproduced by the theoretical radiative efficiency given by Eq. (19) (solid blue line for the central value and the dashed blue lines describe the errors about the central value Table I). From Fig. 3 it is evident that $r_2 > 1.6$ cannot explain the observed η.

The object exhibits strong ballistic jets [113] and the emitted jet power corresponding to $\Gamma = 2$ and $\Gamma = 5$ are reported in Table II. These are associated with an error of $0.3\,dex$ about the central value [97,107]. In Fig. 3 the allowed values of r_2 and a that can explain the emitted jet power along with the positive and the negative errors are depicted by the orange shaded region. The definition of the red solid and dashed lines remain identical to the previous case. The emitted jet power corresponding to $\Gamma = 2$ and $\Gamma = 5$ are reported in Figs. 3(a) and 3(b), respectively. We note from Fig. 3 that the allowed values of spin from the observed jet power and the radiative efficiency, exhibit an overlap in the general relativistic scenario ($r_2 = 0$). We further note that almost the entire allowed range of r_2 can describe the emitted jet power and the restriction on r_2 actually arises from the observed η. Again the zone of intersection between the blue and the orange shaded region represents the values of r_2 and a that describes both the observations. From Figs. 3(a) and 3(b) we note that the allowed values of r_2 correspond to $0 \lesssim r_2 \lesssim 0.8$, which interestingly coincides with the range allowed by the previous source.

3. XTE J1550-564: XTE J1550-564 consists of a binary system with a black hole of mass $9.1 \pm 0.61\ M_\odot$ [117] and a late G- or early K-type star as the companion [118]. The orbital period of the binary is 1.55 days [118]. The distance and inclination of the source are $4.38^{+0.58}_{-0.41}$ kpc and $74.7 \pm 3.8°$ respectively [117]. The spin of the black hole has been estimated both by the continuum fitting and the Fe-line methods. The result obtained from the continuum fitting method corresponds to $-0.11 < a < 0.71$ (90% confidence)[119], with a most likely spin of $a = 0.34$ while Fe-line method gives a spin estimate of $a = 0.55^{+0.15}_{-0.22}$ [119]. In Table I, the spin corresponding to the continuum fitting method has been reported and η is calculated based on this result [103]. The object exhibits a 5 GHz radio-flux density of 0.265 Jy. Using Lorentz factors $\Gamma = 2$ and $\Gamma = 5$, the emitted jet powers are calculated and reported in Table II [103,107]. As before, an error of $0.3\,dex$ is associated with the reported jet powers [97,107]. The emitted jet powers (corresponding to $\Gamma = 2$ and $\Gamma = 5$) along with their errors is compared with the theoretical jet power and the results are presented in Figs. 4(a) and 4(b), respectively. The values of r_2 and a that can explain the emitted jet power within the error bars are denoted by the orange shaded region. The blue shaded region on the other hand, illustrates the allowed values of r_2 and a when the theoretical radiative efficiency equals the observed η. As before $r_2 > 1.6$ cannot explain the observed η while no such restriction on r_2 is imposed from the observed jet power. Once again, the maximum allowed magnitude of r_2 from both the observations is $r_2 \sim 0.9$ [in both Figs. 4(a) and 4(b)]. The range of spin predicted from the jet power (when $r_2 = 0$) is

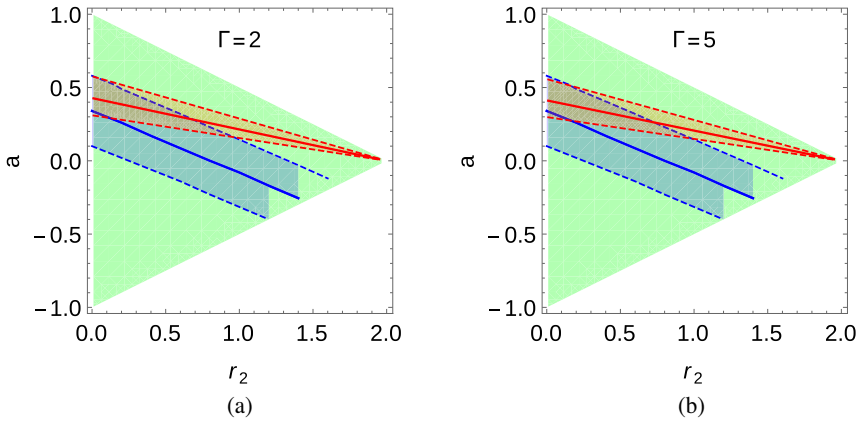

FIG. 4. Black hole source XTE J1550-564. The orange shaded region represents the values of r_2 and a when the theoretical jet power explains the observed luminosity Doppler boosted by the Lorentz factor (a) $\Gamma = 2$ and (b) $\Gamma = 5$. The blue shaded region is associated with the allowed values of r_2 and a that can address the observed η (Table I) within the error bars. The green shaded region indicates the values of r_2 and a giving rise to a real positive event horizon and hence a black hole solution. For more discussion see text.

consistent with the range estimated by the continuum fitting method.

4. GRS 1124-683: this x-ray binary comprises of a black hole of mass $11.0^{+2.1}_{-1.4}\ M_\odot$ [120] and a K-type main sequence star as the companion with an orbital period of 10.4 hours [121]. The distance to the source is $D = 4.95^{+0.69}_{-0.65}$ kpc while the inclination is $i = 43.2^{+2.1\circ}_{-2.7}$ [120]. The spin of the object has been estimated by the continuum fitting method which turns out to be $a = 0.63^{+0.16}_{-0.19}$ [122]. Based on this value for the Kerr parameter, the radiative efficiency has been estimated (Table I). The allowed values of r_2 and a from observed η are described by the blue shaded region in Fig. 5, which reveals that $r_{2,\max} \sim 1.8$.

   The emitted jet power corresponding to this source for $\Gamma = 2$ and $\Gamma = 5$ are reported in Table II. A 0.3 *dex* error on the reported jet power is assumed [97,107]. In Fig. 5 the orange shaded region represents the allowed values of r_2 and a, which can explain the emitted jet power within the error bars. We note that the maximum magnitude of r_2 that can explain both the observed η and $P_{\rm jet}$ corresponds to $r_2 = 1.7$ and $r_2 = 1.5$ for $\Gamma = 2$ and $\Gamma = 5$, respectively. Moreover, unlike the previous black holes, the allowed range of spin that can describe both the observations when $r_2 = 0$ shows an overlap only when $\Gamma = 5$ is considered to compute the emitted jet power from the observed 5 GHz radio-flux density.

5. GRO J1655-40: GRO J1655-40 consists of a black hole of dynamical mass $M = 6.3 \pm 0.5\ M_\odot$ [123] and an F-type secondary star of mass $M_S = 2.34 \pm 0.12\ M_\odot$ with an orbital period of 2.62 days [124]. The distance of the source has been estimated to be $D = 3.2 \pm 0.5$ kpc [125] while its orbital inclination turns out to be $i = 70.2 \pm 1.9°$ [123]. There is a lot of controversy regarding the spin of this source.

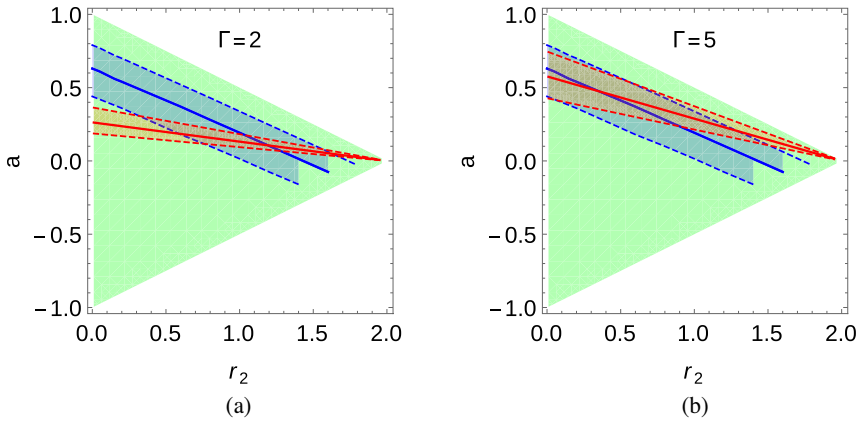

FIG. 5. Black hole source GRS 1124-683. The description of the blue, orange, and the green shaded regions remain the same as in the previous figures. The solid and dashed, red, and blue lines also retain the same definition as in Fig. 2.

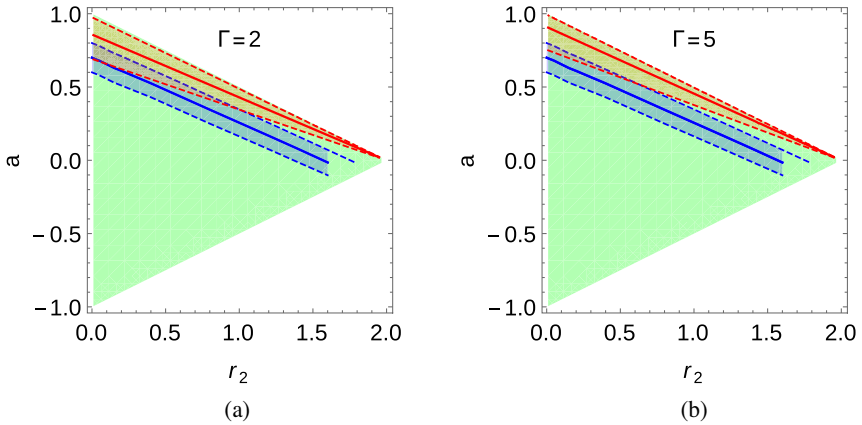

FIG. 6. Black hole source GRO J1655-40. The description of the blue, orange, and the green shaded regions remain the same as in the previous figures. The solid and dashed, red and blue lines also retain the same definition as in Fig. 2.

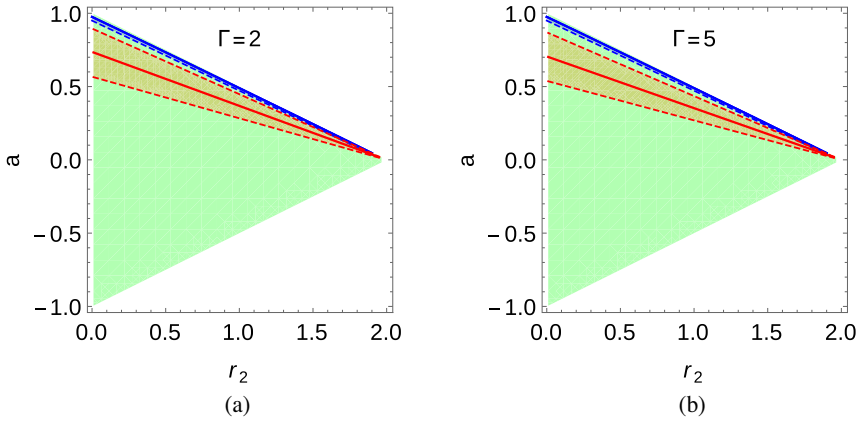

FIG. 7. Black hole source GRS 1915 + 105. The description of the blue, orange, and the green shaded regions remain the same as in the previous figures. The solid and dashed, red and blue lines also retain the same definition as in Fig. 2.

While the continuum fitting method predicts a spin $a \sim 0.65$–0.75 [126], the spin estimated by the Fe-line method is $a > 0.9$ [127]. Based on the quasi-periodic oscillatons observed in the power spectrum of GRO J1655-40, the mass and spin of this object has been constrained to be $M = 5.31 \pm 0.07\ M_\odot$ and $a = 0.290 \pm 0.003$, respectively [128]. In this work however, we consider the spin estimated by the continuum fitting method to evaluate the radiative efficiency. As before, the allowed values of r_2 and a that can explain the observed η within the error bars are shaded in blue in Fig. 6, which shows that $r_{2,\mathrm{max}} \sim 1.8$.

Using the 5 GHz radio-flux density of 2.42 Jy, the emitted jet power has been evaluated assuming Lorentz factors $\Gamma = 2$ and $\Gamma = 5$, which are reported in Table II. These are associated with an error of 0.3 *dex*. In Fig. 6 the orange shaded region represents the values of r_2 and a, which can explain the emitted jet power within the allowed errors. We note that Figs. 6(a) and 6(b) corresponds to the emitted jet power being computed using $\Gamma = 2$ and $\Gamma = 5$, respectively. We note that the observed jet power can be explained by the entire range of r_2. However, if we consider both the observations, $0 \lesssim r_2 \lesssim 1$ if $\Gamma = 2$ and $0 \lesssim r_2 \lesssim 0.7$ when $\Gamma = 5$ is assumed.

6. GRS 1915 + 105: GRS 1915 + 105 is a galactic x-ray binary consisting of a black hole and a K-type star with an orbital period of 34 days [68,129]. The black hole in this x-ray binary has a mass $M = 12.4^{+2.0}_{-1.8}\ M_\odot$ [130]. The distance to the source is $8.6^{+2.0}_{-1.6}$ kpc and the inclination angle is $60 \pm 5°$ [130]. The spin of the black hole estimated by the continuum fitting method turns out to be $a > 0.98$ [131], which is used to estimate the radiative efficiency. In Fig. 7 the blue shaded region bounded by the blue dashed and solid line shows the allowed values of r_2 and a that can explain the observed η. We note that a higher value of r_2 requires a lower spin to reproduce the radiative efficiency.

The object exhibits strong radio jets with 5 GHz radio-flux density being 0.912 Jy [68]. The emitted jet power derived from the flux density after Doppler deboosting with Lorentz factors $\Gamma = 2$ and $\Gamma = 5$ are reported in Table II. As before the error associated with the jet power is $0.3\,dex$. The orange shaded region in Fig. 7 indicates the values of r_2 and a, which can address the observed jet power within the error bars. The solid and the dashed red lines bear the same definition as before. We note from Fig. 7 that almost the entire allowed range of r_2 can explain both the observed $P_{\rm jet}$ and η. Also, when $r_2 \gtrsim 1.5$ both the observations can be simultaneously explained.

B. Implications on the axion-dilaton parameters from observational constraints

We have noted in the last section that the observed radiative efficiency and the jet power can be used to discern the observationally favored magnitude of the dilaton parameter. In order to gain a better understanding on this we note that comparison of the theoretical radiative efficiency [Eq. (19)] and the jet power [Eq. (26)] with the corresponding observations of six microquasars (as depicted in Figs. 2–7) exhibit a few common features:

(i) The observed jet power can be explained by almost the entire allowed range of r_2.
(ii) A higher value of r_2 requires a lower a to explain the observed $P_{\rm jet}$ and η.
(iii) The observational bound on r_2 arises when one tries to reproduce the observed η.
(iv) In most of the cases, when $r_2 = 0$ (general relativistic scenario), the observationally allowed range of a obtained from $P_{\rm jet}$ and η exhibit an overlap.

The above features motivate us to evaluate the chi square as a function of r_2 by comparing $P_{\rm BZ}$ [Eq. (26)] and η [Eq. (19)] with the corresponding observations. This corresponds to the joint χ^2 given by

$$\chi^2(r_2,\{a\}) = \sum_i \frac{\{\eta_{{\rm obs},i} - \eta(r_2,\{a\})\}^2}{\sigma^2_{\eta,i}} + \sum_i \frac{\{P_{\rm jet} - P_{\rm BZ}(r_2,\{a\})\}^2}{\sigma^2_{P,i}}. \quad (30)$$

For every r_2 we vary a in the allowed range: $-(1-\frac{r_2}{2}) \le a \le (1-\frac{r_2}{2})$ (such that the event horizon exists) and compute $\chi^2(r_2,\{a\})$ as in Eq. (30). The spin parameter which gives the minimum χ^2 for the chosen r_2, is considered to be the χ^2 for that r_2. Repeating this procedure for all values of r_2 in the range $0 \le r_2 \le 2$, we obtain the variation of χ^2 with r_2.

Figure 8 shows the variation of the natural logarithm of the χ^2 computed by the above procedure with the dilaton parameter r_2. The red and blue dashed lines are associated with the situation when $P_{\rm BZ}$ in Eq. (30) is compared with the observed $P_{\rm jet}$ corresponding to $\Gamma = 2$ and $\Gamma = 5$, respectively. The black solid line denotes the joint χ^2 when both $\Gamma = 2$ and $\Gamma = 5$ are taken into account. From Fig. 8, we note that while the $\Gamma = 2$ scenario slightly favors a nonzero dilaton parameter ($r_2 \sim 0.1$), the $\Gamma = 5$ case favors the general relativistic scenario. From the joint χ^2, the observationally favored dilaton parameter seems to be $r_2 \sim 0$. The most important outcome of this analysis is that the extreme or even moderate values of r_2 are disfavored from observations related to jet power and radiative efficiency. This implies that pure dilaton black holes (which are nonrotating) are less favored compared to their axion-dilaton counterparts. Also, since the joint χ^2 minimizes around $r_2 \sim 0$, the Kerr black holes seem to explain the observations better than Kerr-Sen black holes.

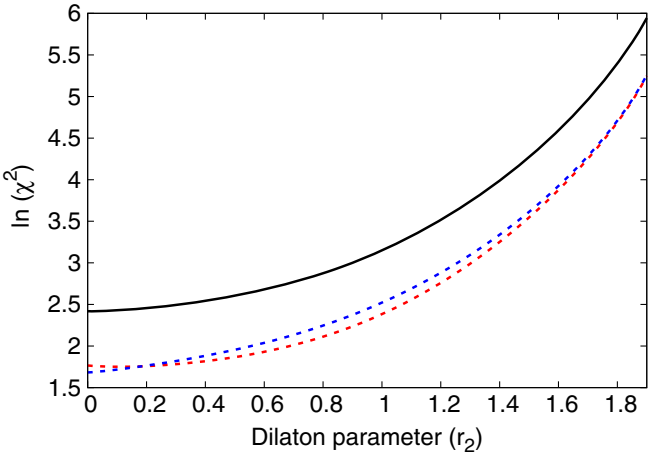

FIG. 8. The figure illustrates the variation of χ^2 with the dilaton parameter r_2 for the sample of microquasars. The red dashed line represents the situation when $P_{\rm jet}$ corresponding to $\Gamma = 2$ is used to compute the χ^2, while the blue dashed line is associated with the scenario when $P_{\rm jet}$ corresponding to $\Gamma = 5$ is considered for evaluating the χ^2. The black solid line denotes the joint χ^2 when both $\Gamma = 2$ and $\Gamma = 5$ are taken into account. For more discussions see text.

V. SUMMARY AND CONCLUDING REMARKS

In this work we aim to discern the imprints of Einstein-Maxwell dilaton-axion gravity from observations related to jet power and radiative efficiency of microquasars. The EMDA gravity essentially arises in the low energy effective action of superstring theories and investigating the observational signatures of the same is important as it can provide an indirect testbed for string theory. The theoretical implications of this model has been explored extensively in the past and the exact, stationary and axisymmetric black hole solution in this theory has been worked out. Such a solution corresponds to the Kerr-Sen spacetime which

contains dilaton charges while the axionic field renders angular momentum to such black holes.

The observational signatures of the Kerr-Sen spacetime has been explored in the context of strong gravitational lensing and black hole shadows [59,63–65]. Therefore, in this work we investigate the role of the Kerr-Sen background in affecting the jet power and the radiative efficiency derived from the continuum spectrum associated with the black holes. The transient jet power and the peak emission of the continuum spectrum from the accretion disk are sensitive to the background spacetime and hence can be used as important observational tools to probe the nature of strong gravity.

The power associated with transient jets is computed based on the Blandford-Zanjeck model that explicitly reveals the dependence of the background metric on the jet power. This is then compared with the emitted jet power of a sample of microquasars estimated from the peak 5 GHz radio flux density which is Doppler boosted by Lorentz factors $\Gamma = 2$ and $\Gamma = 5$ and scaled by the distance to obtain the associated luminosity. The jet power estimated by this method turns out to be model independent and hence sufficiently reliable [97]. If the background is governed by the Kerr metric then such an observation can be used to determine the black hole spins [97]. In the event the background corresponds to the Kerr-Sen spacetime, the allowed values of the spin and the dilaton parameters can be determined based on the observed jet power. A departure from general relativity therefore introduces a degeneracy between the metric parameters, and only a combination of these parameters can be constrained.

The radiative efficiency, the second metric dependent quantity used in this work, is calculated based on the Novikov-Thorne model for thin accretion disk. This is subsequently compared with the observed radiative efficiency of the same sample of microquasars whose jet powers have been evaluated. The radiative efficiency is derived from the peak emission of the continuum spectrum and assuming general relativity, it can be used to constrain the spins of the underlying black holes. This forms the basis of the Continuum-Fitting method for determining the spins of the microquasars. In the event the background is governed by the Kerr-Sen spacetime, the radiative efficiency can be used to determine the allowed values of spin and dilaton parameters for each of the black holes.

We note that the dilaton-axion black hole can explain the observed jet power and the radiative efficiency of the microquasars. Although, in this case the jet is powered by the interplay between the axion and the dilaton fields. For each of the microquasars the spin and the dilaton parameters which can explain both the observations are considered. It turns out that in most of the cases large values of the dilaton parameters, viz., $r_2 \gtrsim 1$ are generally disfavored. A greater axionic field strength requires a smaller dilatonic charge of the black hole to reproduce these two observations. A chi-square analysis is performed where the observed jet power and the radiative efficiency of the microquasars are compared with the corresponding theoretical estimates depending on the metric parameters. Such an analysis clearly reveals that pure dilaton black holes are observationally less favored compared to their axion-dilaton counterparts. Moreover, since the chi-square minimizes when $r_2 \simeq 0$, the Kerr black holes seem to be observationally more favored compared to the Kerr-Sen black holes. We have noted earlier that $r_2/\mathcal{M} = \frac{\alpha' Q^2}{8\mathcal{M}^2}$. Therefore obtaining $r_2 \simeq 0$ from the observations implies $Q \simeq 0$ since $\alpha' \simeq 0$ would lead to gauge anomaly. Since astrophysical black holes are expected to carry negligible charge [70], our result $r_2 \simeq 0$ also implies $Q \simeq 0$, in which case we retrieve the Kerr metric. However, it is important to note that observational validation of the Kerr scenario does not necessarily validate general relativity since the Kerr metric also arises as black hole solution for several alternative gravity scenarios [50,72,132].

In the Kerr scenario, the axion or the Kalb-Ramond field exhibit a vanishing field strength whose suppression has been observed in several other physical scenarios, e.g., in the context of higher curvature gravity where the related scalar degrees of freedom reduces the coupling of such a field with the Standard Model fermions [133,134], in the warped braneworld scenario [135] with bulk Kalb-Ramond fields [136,137] and the related stabilization of the modulus [138] and in the inflationary era induced by higher curvature gravity [139,140] and higher dimensions [141]. A similar conclusion $r_2 \simeq 0.2$ (which is close to $r_2 \simeq 0$) has been independently achieved by comparing the theoretical luminosity from the accretion disk in the Kerr-Sen background with the optical observations of quasars [142]. This result can be further verified with the availability of a larger observational sample or by considering more observations in the electromagnetic domain, e.g., quasiperiodic oscillations or black hole shadow, which will be reported in a future work.

ACKNOWLEDGMENTS

The research of S. S. G. is supported by the Science and Engineering Research Board-Extra Mural Research Grant No. EMR/2017/001372, Government of India.

APPENDIX A: DERIVATION OF THE JET POWER IN THE BLANDFORD-ZNAJECK MODEL

In this section we derive the jet power in the Blandford-Znajeck model assuming a general stationary, axisymmetric spacetime. We have already discussed that the Blandford-Znajeck model assumes a force-free magnetosphere where the particle inertia is neglected compared to the energy-momentum tensor due to the electromagnetic fields, such that

$$T^{\rm tot}_{\mu\nu} = T^{\rm EM}_{\mu\nu} + T^{\rm matter}_{\mu\nu} \approx T^{\rm EM}_{\mu\nu} \tag{A1}$$

where

$$T^{\rm EM}_{\mu\nu} = F_{\mu\rho}F^{\rho}_{\nu} - \frac{1}{4}g_{\mu\nu}F^{\alpha\beta}F_{\alpha\beta} \tag{A2}$$

satisfies the conservation equation

$$\nabla^{\mu}T^{\rm EM}_{\mu\nu} = 0. \tag{A3}$$

In Eq. (A2), $F_{\mu\nu} = \partial_{\mu}A_{\nu} - \partial_{\nu}A_{\mu}$ is the Faraday tensor and A_{μ} is the gauge field. In a force-free magnetosphere the Faraday tensor satisfies the relation [70],

$$F_{\mu\nu}J^{\nu} = 0 \tag{A4}$$

such that

$$A_{t,r}J^{r} + A_{t,\theta}J^{\theta} = 0, \tag{A4a}$$

$$A_{t,r}J^{t} + A_{\phi,r}J^{\phi} + B_{\phi}J^{\theta} = 0, \tag{A4b}$$

$$A_{t,\theta}J^{t} + A_{\phi,\theta}J^{\phi} + B_{\phi}J^{r} = 0, \tag{A4c}$$

$$A_{\phi,r}J^{r} + A_{\phi,\theta}J^{\theta} = 0, \tag{A4d}$$

and J^{ν} is the current four vector. From Eqs. (A4a) and (A4d) one can define the electromagnetic angular velocity $\omega(r,\theta)$, where

$$\frac{A_{t,r}}{A_{\phi,r}} = \frac{A_{t,\theta}}{A_{\phi,\theta}} = -\omega(r,\theta). \tag{A5}$$

Assuming the validity of the force-free condition and that A_{μ} is stationary and axisymmetric one can write the Faraday tensor in the form

$$F_{\mu\nu} = \sqrt{-g}\begin{pmatrix} 0 & -\omega B^{\theta} & \omega B^{r} & 0 \\ \omega B^{\theta} & 0 & B^{\phi} & -B^{\theta} \\ -\omega B^{r} & -B^{\phi} & 0 & B^{r} \\ 0 & B^{\theta} & -B^{r} & 0 \end{pmatrix}. \tag{A6}$$

The power associated with the relativistic jet in the context of the Blandford-Znajeck model is given by

$$P_{\rm BZ} = 4\pi\int_{0}^{\pi/2}\sqrt{-g}T^{r}_{t}d\theta, \tag{A7}$$

which takes into account the fact that the jets are bipolar. In Eq. (A7) T^{r}_{t} represents the radial component of the Poynting flux. From Eq. (A2) it can be shown that the radial component of the Poynting flux assumes the form

$$T^{r}_{t} = g^{rr}g^{\theta\theta}F_{r\theta}F_{\theta t} - g^{rt}g^{\theta\theta}F^{2}_{t\theta} + g^{r\phi}g^{\theta\theta}F_{\phi\theta}F_{\theta t} \tag{A8}$$

such that the information of the metric enters both through its determinant and through T^{r}_{t} in the jet power.

APPENDIX B: JET POWER IN THE EINSTEIN-MAXWELL-DILATON-AXION GRAVITY

In this section we derive the jet power in the Kerr-Sen background arising in Einstein-Maxwell-dilaton-axion gravity. We assume that the jet launching radius corresponds to the event horizon and hence the first term in Eq. (A8) vanishes. In order to derive the jet power one requires that the metric is regular at the horizon. As a result we express our metric given by Eq. (10) in the Kerr-Schild coordinates,

$$\begin{aligned} ds^2 = &\left(-1 + \frac{2r}{\tilde{\Sigma}}\right)dt^2 + \frac{4r}{\tilde{\Sigma}}dtdr - \sin^2\theta\frac{4ar}{\tilde{\Sigma}}dtd\phi \\ &+ \left(1 + \frac{2r}{\tilde{\Sigma}}\right)dr^2 - 2a\sin^2\theta\left(1 + \frac{2r}{\tilde{\Sigma}}\right)drd\phi + \tilde{\Sigma}d\theta^2 \\ &+ \sin^2\theta\left(a^2 + r(r + r_2) + 2\sin^2\theta\frac{a^2 r}{\tilde{\Sigma}}\right)d\phi^2. \end{aligned} \tag{B1}$$

Using Eqs. (A8) and (B1) the radial component of the Poynting flux is given by

$$T^{r}_{t} = 2r_H M\sin^2\theta(B^{r})^2\omega[\Omega_H - \omega]|_{r=r_H}, \tag{B2}$$

where

$$r_H = 1 - \frac{r_2}{2} + \sqrt{\left(1 - \frac{r_2}{2}\right)^2 - a^2} \quad \text{and} \tag{B3}$$

$$\Omega_H = \left(-\frac{g_{t\phi}}{g_{\phi\phi}}\right)\Big|_{r=r_H} \tag{B4}$$

is the horizon radius and the angular velocity of the event horizon, respectively. It is important to note that, for the metric in Eq. (B1),

$$\Omega_H = \left(-\frac{g_{t\phi}}{g_{\phi\phi}}\right)\Big|_{r=r_H} = \left(\frac{g^{r\phi}}{g^{rt}}\right)\Big|_{r=r_H} = \frac{a}{2r_H} \tag{B5}$$

and $\sqrt{-g} = \tilde{\Sigma}\sin\theta$.

At this stage, it is impossible to calculate the jet power without knowing the form of ω and B^{r}. This requires solving Eq. (A3) which is quite nontrivial. Therefore, we follow the approach adopted by [101,102], where $\omega = \Omega_H/2$ is assumed. This can be obtained by maximizing the radial Poynting flux T^{r}_{t} in Eq. (B2) with respect to ω [102]. With this assumption, Eq. (B2) is given by

$$T^{r}_{t} = 2r_H M\sin^2\theta(B^{r})^2\frac{\Omega^2_H}{4}. \tag{B6}$$

In the stationary and axisymmetric spacetime at a constant (r,θ), the physical quantities are invariant along the azimuthal direction, the so-called m loops [143]. Consequently, by applying Stoke's law along one of these "m loops" the magnetic flux Φ_B through it is given by

$$\Phi_B = \int \vec{B}.d\vec{S} = \int (\vec{\nabla}\times\vec{A}).d\vec{S} = \oint \vec{A}.d\vec{l} = 2\pi A_\phi. \quad \text{(B7)}$$

Further, from Eq. (A6) it is clear that $F_{\theta\phi} = A_{\phi,\theta} = \sqrt{-g}B^r$ such that

$$\Phi_B = 2\pi A_\phi = 2\pi \int_0^\pi \sqrt{-g}|B^r|d\theta = 2\pi\Psi. \quad \text{(B8)}$$

Therefore, the azimuthal component of the vector potential A_ϕ is directly related to the magnetic flux through the m loops and is denoted by Ψ. Assuming that the magnetic flux Ψ approximately follows the split-monopole profile it can be shown that [102]

$$B^r = \frac{\Psi_{\rm tot}}{r^2}, \quad \text{(B9)}$$

where terms of the order Ω_H^2 and higher are neglected. Substituting Eqs. (B9) and (B6) in Eq. (A7) and evaluating it at the horizon radius, it can be shown that

$$P_{\rm BZ} = k\Phi_{\rm tot}^2\Omega_H^2 \quad \text{(B10)}$$

when terms of order Ω_H^4 and higher are neglected [102]. In Eq. (B10) $\Phi_{\rm tot}$ represents the magnetic flux threading the event horizon.

[1] C. M. Will, Was Einstein right?, Ann. Phys. (Berlin) **15**, 19 (2006).
[2] C. M. Will, *Theory and Experiment in Gravitational Physics*, 2nd ed. (Cambridge University Press, Cambridge, 1993), https://doi.org/10.1017/9781316338612.
[3] C. M. Will, The Confrontation between general relativity and experiment, Living Rev. Relativity **9**, 3 (2006).
[4] E. Berti *et al.*, Testing general relativity with present and future astrophysical observations, Classical Quant. Grav. **32**, 243001 (2015).
[5] B. P. Abbott *et al.* (LIGO Scientific and VIRGO Collaborations), GW170104: Observation of a 50-Solar-Mass Binary Black Hole Coalescence at Redshift 0.2, Phys. Rev. Lett. **118**, 221101 (2017); Erratum, **121**, 129901 (2018).
[6] B. P. Abbott *et al.* (LIGO Scientific and Virgo Collaborations), Binary Black Hole Mergers in the first Advanced LIGO Observing Run, Phys. Rev. X **6** (2016) 041015; Erratum, Phys. Rev. X **8**, 039903 (2018).
[7] B. P. Abbott *et al.* (LIGO Scientific and Virgo Collaborations), GW151226: Observation of Gravitational Waves from a 22-Solar-Mass Binary Black Hole Coalescence, Phys. Rev. Lett. **116**, 241103 (2016).
[8] B. P. Abbott *et al.* (LIGO Scientific and Virgo Collaborations), Tests of general relativity with GW150914, Phys. Rev. Lett. **116**, 221101 (2016); Erratum, Phys. Rev. Lett. **121**, 129902 (2018).
[9] B. P. Abbott *et al.* (LIGO Scientific and Virgo Collaborations), Observation of Gravitational Waves from a Binary Black Hole Merger, Phys. Rev. Lett. **116**, 061102 (2016).
[10] V. L. Fish, K. Akiyama, K. L. Bouman, A. A. Chael, M. D. Johnson, S. S. Doeleman, L. Blackburn, J. F. C. Wardle, and W. T. Freeman (Event Horizon Telescope Collaboration), Observing and imaging active galactic nuclei with the event horizon telescope, Galaxies **4**, 54 (2016).
[11] K. Akiyama *et al.* (Event Horizon Telescope Collaboration), First M87 event horizon telescope results. I. The shadow of the supermassive black hole, Astrophys. J. **875**, L1 (2019).
[12] K. Akiyama *et al.* (Event Horizon Telescope Collaboration), First M87 Event Horizon Telescope Results. II. Array and instrumentation, Astrophys. J. **875**, L2 (2019).
[13] K. Akiyama *et al.* (Event Horizon Telescope Collaboration), First M87 event horizon telescope results. III. Data processing and calibration, Astrophys. J. **875**, L3 (2019).
[14] K. Akiyama *et al.* (Event Horizon Telescope Collaboration), First M87 event horizon telescope results. IV. Imaging the central supermassive black hole, Astrophys. J. **875**, L4 (2019).
[15] K. Akiyama *et al.* (Event Horizon Telescope Collaboration), First M87 event horizon telescope results. V. Physical origin of the asymmetric ring, Astrophys. J. **875**, L5 (2019).
[16] K. Akiyama *et al.* (Event Horizon Telescope Collaboration), First M87 event horizon telescope results. VI. The shadow and mass of the central black hole, Astrophys. J. **875**, L6 (2019).
[17] R. Penrose, Gravitational Collapse and Space-Time Singularities, Phys. Rev. Lett. **14**, 57 (1965).
[18] S. W. Hawking, Breakdown of predictability in gravitational collapse, Phys. Rev. D **14**, 2460 (1976).
[19] D. Christodoulou, The formation of black holes and singularities in spherically symmetric gravitational collapse, Commun. Pure Appl. Math. **44**, 339 (1991).
[20] J. Bekenstein and M. Milgrom, Does the missing mass problem signal the breakdown of Newtonian gravity?, Astrophys. J. **286**, 7 (1984).
[21] S. Perlmutter *et al.* (Supernova Cosmology Project Collaboration), Measurements of Omega and Lambda from 42 high redshift supernovae, Astrophys. J. **517**, 565 (1999).

[22] A. G. Riess *et al.* (Supernova Search Team Collaboration), Observational evidence from supernovae for an accelerating universe and a cosmological constant, Astron. J. **116**, 1009 (1998).
[23] C. Rovelli, Black Hole Entropy from Loop Quantum Gravity, Phys. Rev. Lett. **77**, 3288 (1996).
[24] F. Dowker, Causal sets and the deep structure of spacetime, in *100 Years of Relativity: Space-Time Structure: Einstein and Beyond*, edited by A. Ashtekar (2005), pp. 445–464.
[25] A. Ashtekar, T. Pawlowski, and P. Singh, Quantum Nature of the Big Bang, Phys. Rev. Lett. **96**, 141301 (2006).
[26] D. Kothawala, Minimal length and small scale structure of spacetime, Phys. Rev. D **88**, 104029 (2013).
[27] T. Shiromizu, K.-i. Maeda, and M. Sasaki, The Einstein equation on the 3-brane world, Phys. Rev. D **62**, 024012 (2000).
[28] N. Dadhich, R. Maartens, P. Papadopoulos, and V. Rezania, Black holes on the brane, Phys. Lett. B **487**, 1 (2000).
[29] T. Harko and M. Mak, Vacuum solutions of the gravitational field equations in the brane world model, Phys. Rev. D **69**, 064020 (2004).
[30] T. R. P. Carames, M. E. X. Guimaraes, and J. M. Hoff da Silva, Effective gravitational equations for $f(R)$ brane-world models, Phys. Rev. D **87**, 106011 (2013).
[31] T. Kobayashi, T. Shiromizu, and N. Deruelle, Low energy effective gravitational equations on a Gauss-Bonnet brane, Phys. Rev. D **74**, 104031 (2006).
[32] S. Chakraborty and S. SenGupta, Spherically symmetric brane spacetime with bulk $f(\mathcal{R})$ gravity, Eur. Phys. J. C **75**, 11 (2015).
[33] S. Chakraborty and S. SenGupta, Effective gravitational field equations on m-brane embedded in n-dimensional bulk of Einstein and $f(\mathcal{R})$ gravity, Eur. Phys. J. C **75**, 538 (2015).
[34] S. Nojiri and S. D. Odintsov, Modified gravity with negative and positive powers of the curvature: Unification of the inflation and of the cosmic acceleration, Phys. Rev. D **68**, 123512 (2003).
[35] S. Nojiri and S. D. Odintsov, Modified f(R) gravity consistent with realistic cosmology: From matter dominated epoch to dark energy universe, Phys. Rev. D **74**, 086005 (2006).
[36] S. Capozziello, S. Nojiri, S. D. Odintsov, and A. Troisi, Cosmological viability of f(R)-gravity as an ideal fluid and its compatibility with a matter dominated phase, Phys. Lett. B **639**, 135 (2006).
[37] C. Lanczos, Electricity as a natural property of Riemannian geometry, Rev. Mod. Phys. **39**, 716 (1932).
[38] C. Lanczos, A Remarkable property of the Riemann-Christoffel tensor in four dimensions, Ann. Math. **39**, 842 (1938).
[39] D. Lovelock, The Einstein tensor and its generalizations, J. Math. Phys. (N.Y.) **12**, 498 (1971).
[40] T. Padmanabhan and D. Kothawala, Lanczos-Lovelock models of gravity, Phys. Rep. **531**, 115 (2013).
[41] G. W. Horndeski, Second-order scalar-tensor field equations in a four-dimensional space, Int. J. Theor. Phys. **10**, 363 (1974).
[42] T. P. Sotiriou and S.-Y. Zhou, Black Hole Hair in Generalized Scalar-Tensor Gravity, Phys. Rev. Lett. **112**, 251102 (2014).
[43] E. Babichev, C. Charmousis, and A. Lehbel, Black holes and stars in Horndeski theory, Classical Quant. Grav. **33**, 154002 (2016).
[44] C. Charmousis and M. Tsoukalas, Lovelock Galileons and black holes, Phys. Rev. D **92**, 104050 (2015).
[45] S. Bhattacharya and S. Chakraborty, Constraining some Horndeski gravity theories, Phys. Rev. D **95**, 044037 (2017).
[46] P. Horava and E. Witten, Heterotic and type I string dynamics from eleven-dimensions, Nucl. Phys. **B460**, 506 (1996).
[47] P. Horava and E. Witten, Eleven-dimensional supergravity on a manifold with boundary, Nucl. Phys. **B475**, 94 (1996).
[48] J. Polchinski, String Theory. Vol. 1: An Introduction to the Bosonic String, *Cambridge Monographs on Mathematical Physics* (Cambridge University Press, Cambridge, England, 2007).
[49] J. Polchinski, String Theory. Vol. 2: Superstring Theory and Beyond, *Cambridge Monographs on Mathematical Physics* (Cambridge University Press, Cambridge, England, 2007).
[50] A. Sen, Rotating Charged Black Hole Solution in Heterotic String Theory, Phys. Rev. Lett. **69**, 1006 (1992).
[51] M. Rogatko, Positivity of energy in Einstein-Maxwell axion dilaton gravity, Classical Quant. Grav. **19**, 5063 (2002).
[52] J. Sonner and P. K. Townsend, Recurrent acceleration in dilaton-axion cosmology, Phys. Rev. D **74**, 103508 (2006).
[53] R. Catena and J. Moller, Axion-dilaton cosmology and dark energy, J. Cosmol. Astropart. Phys. 03 (2008) 012.
[54] G. Gibbons and K.-i. Maeda, Black holes and membranes in higher dimensional theories with dilaton fields, Nucl. Phys. **B298**, 741 (1988).
[55] D. Garfinkle, G. T. Horowitz, and A. Strominger, Charged black holes in string theory, Phys. Rev. D **43**, 3140 (1991); Erratum, Phys. Rev. D **45**, 3888 (1992).
[56] G. T. Horowitz and A. Strominger, Black strings and P-branes, Nucl. Phys. **B360**, 197 (1991).
[57] R. Kallosh and T. Ortin, Charge quantization of axion-dilaton black holes, Phys. Rev. D **48**, 742 (1993).
[58] *Black Holes: The Membrane Paradigm*, edited by K. S. Thorne, R. Price, and D. Macdonald (Yale University Press, New Haven, USA, 1986), p. 367, ISBN 978-0-300-03770-8.
[59] K. Hioki and U. Miyamoto, Hidden symmetries, null geodesics, and photon capture in the Sen black hole, Phys. Rev. D **78**, 044007 (2008).
[60] P. Pradhan, Thermodynamic products for Sen black hole, Eur. Phys. J. C **76**, 131 (2016).
[61] M. Guo, S. Song, and H. Yan, Observational signature of a near-extremal Kerr-Sen black hole in the heterotic string theory, Phys. Rev. D **101**, 024055 (2020).
[62] R. Uniyal, H. Nandan, and K. D. Purohit, Null geodesics and observables around the Kerr–Sen black hole, Classical Quant. Grav. **35**, 025003 (2018).

[63] G. N. Gyulchev and S. S. Yazadjiev, Kerr-Sen dilaton-axion black hole lensing in the strong deflection limit, Phys. Rev. D **75**, 023006 (2007).
[64] J. An, J. Peng, Y. Liu, and X.-H. Feng, Kerr-Sen black hole as accelerator for spinning particles, Phys. Rev. D **97**, 024003 (2018).
[65] Z. Younsi, A. Zhidenko, L. Rezzolla, R. Konoplya, and Y. Mizuno, New method for shadow calculations: Application to parametrized axisymmetric black holes, Phys. Rev. D **94**, 084025 (2016).
[66] Y. Mizuno, Z. Younsi, C. M. Fromm, O. Porth, M. De Laurentis, H. Olivares, H. Falcke, M. Kramer, and L. Rezzolla, The current ability to test theories of gravity with black hole shadows, Nat. Astron. **2**, 585 (2018).
[67] A. Narang, S. Mohanty, and A. Kumar, Test of Kerr-Sen metric with black hole observations, arXiv:2002.12786.
[68] I. Mirabel and L. Rodriguez, A Superluminal source in the galaxy, Nature (London) **371**, 46 (1994).
[69] R. Fender and T. Belloni, GRS 1915 + 105 and the disc-jet coupling in accreting black hole systems, Annu. Rev. Astron. Astrophys. **42**, 317 (2004).
[70] R. D. Blandford and R. L. Znajek, Electromagnetic extractions of energy from Kerr black holes, Mon. Not. R. Astron. Soc. **179**, 433 (1977).
[71] I. D. Novikov and K. S. Thorne, Astrophysics and black holes, in *Proceedings, Ecole d'Et de Physique Thorique: Les Astres Occlus: Les Houches, France, 1972* (1973), pp. 343–550.
[72] B. A. Campbell, N. Kaloper, R. Madden, and K. A. Olive, Physical properties of four-dimensional superstring gravity black hole solutions, Nucl. Phys. **B399**, 137 (1993).
[73] A. Sen, Black hole solutions in heterotic string theory on a torus, Nucl. Phys. **B440**, 421 (1995).
[74] D. J. Gross and J. H. Sloan, The quartic effective action for the heterotic string, Nucl. Phys. **B291**, 41 (1987).
[75] A. Garcia, D. Galtsov, and O. Kechkin, Class of Stationary Axisymmetric Solutions of the Einstein-Maxwell Dilaton-Axion Field Equations, Phys. Rev. Lett. **74**, 1276 (1995).
[76] A. Ghezelbash and H. Siahaan, Hidden and generalized conformal symmetry of Kerr-Sen spacetimes, Classical Quant. Grav. **30**, 135005 (2013).
[77] C. Bernard, Stationary charged scalar clouds around black holes in string theory, Phys. Rev. D **94**, 085007 (2016).
[78] G. D. Moore and A. E. Nelson, Lower bound on the propagation speed of gravity from gravitational Cherenkov radiation, J. High Energy Phys. 09 (2001) 023.
[79] P. M. Chesler and A. Loeb, Constraining Relativistic Generalizations of Modified Newtonian Dynamics with Gravitational Waves, Phys. Rev. Lett. **119**, 031102 (2017).
[80] C. Ganguly and S. SenGupta, Penrose process in a charged axion-dilaton coupled black hole, Eur. Phys. J. C **76**, 213 (2016).
[81] S. Yazadjiev, Exact static solutions in four-dimensional Einstein-Maxwell dilaton gravity, Int. J. Mod. Phys. D **08**, 635 (1999).
[82] E. Newman and A. Janis, Note on the Kerr spinning particle metric, J. Math. Phys. (N.Y.) **6**, 915 (1965).
[83] I. Mirabel and L. Rodriguez, Sources of relativistic jets in the galaxy, Annu. Rev. Astron. Astrophys. **37**, 409 (1999).
[84] V. Cardoso, O. J. Dias, G. S. Hartnett, M. Middleton, P. Pani, and J. E. Santos, Constraining the mass of dark photons and axion-like particles through black-hole superradiance, J. Cosmol. Astropart. Phys. 03 (2018) 043.
[85] A. Arvanitaki and S. Dubovsky, Exploring the string axiverse with precision black hole physics, Phys. Rev. D **83**, 044026 (2011).
[86] M. Baryakhtar, R. Lasenby, and M. Teo, Black hole superradiance signatures of ultralight vectors, Phys. Rev. D **96**, 035019 (2017).
[87] R. Brito, S. Ghosh, E. Barausse, E. Berti, V. Cardoso, I. Dvorkin, A. Klein, and P. Pani, Stochastic and Resolvable Gravitational Waves from Ultralight Bosons, Phys. Rev. Lett. **119**, 131101 (2017).
[88] R. Brito, S. Ghosh, E. Barausse, E. Berti, V. Cardoso, I. Dvorkin, A. Klein, and P. Pani, Gravitational wave searches for ultralight bosons with LIGO and LISA, Phys. Rev. D **96**, 064050 (2017).
[89] Y. Huang, D.-J. Liu, X.-H. Zhai, and X.-Z. Li, Scalar clouds around Kerr–Sen black holes, Classical Quant. Grav. **34**, 155002 (2017).
[90] R. Cayuso, O. J. Dias, F. Gray, D. Kubizňák, A. Margalit, J. E. Santos, R. Gomes Souza, and L. Thiele, Massive vector fields in Kerr-Newman and Kerr-Sen black hole spacetimes, J. High Energy Phys. 04 (2020) 159.
[91] C. Bambi, Testing the Kerr-nature of stellar-mass black hole candidates by combining the continuum-fitting method and the power estimate of transient ballistic jets, Phys. Rev. D **85**, 043002 (2012).
[92] D. N. Page and K. S. Thorne, Disk-accretion onto a black hole. Time-averaged structure of accretion disk, Astrophys. J. **191**, 499 (1974).
[93] I. Banerjee, S. Chakraborty, and S. SenGupta, Decoding signatures of extra dimensions and estimating spin of quasars from the continuum spectrum, Phys. Rev. D **100**, 044045 (2019).
[94] L. Brenneman, Measuring supermassive black hole spins in active galactic nuclei, arXiv:1309.6334.
[95] J. E. McClintock, R. Narayan, and J. F. Steiner, Black hole spin via continuum fitting and the role of spin in powering transient jets, Space Sci. Rev. **183**, 295 (2014).
[96] S. Markoff, M. A. Nowak, and J. Wilms, Going with the flow: Can the base of jets subsume the role of compact accretion disk coronae?, Astrophys. J. **635**, 1203 (2005).
[97] R. Narayan and J. E. McClintock, Observational evidence for a correlation between jet power and black hole spin, Mon. Not. R. Astron. Soc. **419**, L69 (2012).
[98] B. Punsly and F. V. Coroniti, Ergosphere-driven winds, Astrophys. J. **354**, 583 (1990).
[99] M. Takahashi, S. Nitta, Y. Tatematsu, and A. Tomimatsu, Magnetohydrodynamic flows in Kerr geometry: Energy extraction from black holes, Astrophys. J. **363**, 206 (1990).
[100] S. Koide, Magnetic extraction of black hole rotational energy: Method and results of general relativistic magnetohydrodynamic simulations in Kerr space-time, Phys. Rev. D **67**, 104010 (2003).
[101] K. Tanabe and S. Nagataki, Extended monopole solution of the Blandford-Znajek mechanism: Higher order terms for a Kerr parameter, Phys. Rev. D **78**, 024004 (2008).

[102] A. Tchekhovskoy, R. Narayan, and J. C. McKinney, Black hole spin and the radio loud/quiet dichotomy of active galactic nuclei, Astrophys. J. **711**, 50 (2010).
[103] G. Pei, S. Nampalliwar, C. Bambi, and M. J. Middleton, Blandford-Znajek mechanism in black holes in alternative theories of gravity, Eur. Phys. J. C **76**, 534 (2016).
[104] J. F. Steiner, J. E. McClintock, and R. Narayan, Jet power and black hole spin: Testing an empirical relationship and using it to predict the spins of six black holes, Astrophys. J. **762**, 104 (2013).
[105] R. P. Fender, T. Belloni, and E. Gallo, Towards a unified model for black hole x-ray binary jets, Mon. Not. R. Astron. Soc. **355**, 1105 (2004).
[106] R. Fender, in *Jets From X-Ray Binaries*, Vol. 39 (2006), pp. 381–419.
[107] M. Middleton, J. Miller-Jones, and R. Fender, The low or retrograde spin of the first extragalactic microquasar: Implications for Blandford–Znajek powering of jets, Mon. Not. R. Astron. Soc. **439**, 1740 (2014).
[108] A. G. Cantrell, C. D. Bailyn, J. A. Orosz, J. E. McClintock, R. A. Remillard, C. S. Froning, J. Neilsen, D. M. Gelino, and L. Gou, The inclination of the soft x-ray transient A0620–00 and the mass of its black hole, Astrophys. J. **710**, 1127 (2010).
[109] C. Foellmi, What is the closest black-hole to the sun?, New Astron. **14**, 674 (2009).
[110] J. E. McClintock and R. A. Remillard, The black hole binary A0620-00, Astrophys. J. **308**, 110 (1986).
[111] L. Gou, J. E. McClintock, J. F. Steiner, R. Narayan, A. G. Cantrell, C. D. Bailyn, and J. A. Orosz, The spin of the black hole in the soft x-ray transient A0620–00, Astrophys. J. **718**, L122 (2010).
[112] E. Kuulkers, R. P. Fender, R. E. Spencer, R. J. Davis, and I. Morison, Multiple ejections during the 1975 outburst of a0620-00, Mon. Not. R. Astron. Soc. **306**, 919 (1999).
[113] J. F. Steiner, J. E. McClintock, and M. J. Reid, The distance, inclination, and spin of the black hole microquasar H1743-322, Astrophys. J. **745**, L7 (2012).
[114] J. Petri, A new model for QPOs in accreting black holes: Application to the microquasar GRS $1915+105$, Astrophys. Space Sci. **318**, 181 (2008).
[115] S. Chaty, A. Muoz Arjonilla, and G. Dubus, Infrared study of H 1743-322 in outburst: A radio-quiet and NIR-dim microquasar, Astron. Astrophys. **577**, A101 (2015).
[116] P. Jonker *et al.*, Following the 2008 outburst decay of the black hole candidate H1743-322 in X-ray and radio, Mon. Not. R. Astron. Soc. **401**, 1255 (2010).
[117] J. A. Orosz, J. F. Steiner, J. E. McClintock, M. A. Torres, R. A. Remillard, C. D. Bailyn, and J. M. Miller, An improved dynamical model for the microquasar XTE J1550-564, Astrophys. J. **730**, 75 (2011).
[118] J. A. Orosz, P. J. Groot, M. van der Klis, J. E. McClintock, M. R. Garcia, P. Zhao, R. K. Jain, C. D. Bailyn, and R. A. Remillard, Dynamical evidence for a black hole in the microquasar XTE J1550-564, Astrophys. J. **568**, 845 (2002).
[119] J. F. Steiner, R. C. Reis, J. E. McClintock, R. Narayan, R. A. Remillard, J. A. Orosz, L. Gou, A. C. Fabian, and M. A. Torres, The Spin of the Black Hole Microquasar XTE J1550-564 via the continuum-fitting and fe-line methods, Mon. Not. R. Astron. Soc. **416**, 941 (2011).
[120] J. Wu, J. A. Orosz, J. E. McClintock, I. Hasan, C. D. Bailyn, L. Gou, and Z. Chen, The mass of the black hole in the x-ray binary Nova Muscae 1991, Astrophys. J. **825**, 46 (2016).
[121] R. A. Remillard, J. E. McClintock, and C. D. Bailyn, Evidence for a black hole in the x-ray binary Nova MUSCAE 1991, Astrophys. J. Lett. **399**, L145 (1992).
[122] Z. Chen, L. Gou, J. E. McClintock, J. F. Steiner, J. Wu, W. Xu, J. Orosz, and Y. Xiang, The spin of the black hole in the x-ray binary Nova Muscae 1991, Astrophys. J. **825**, 45 (2016).
[123] J. Greene, C. D. Bailyn, and J. A. Orosz, Optical and infrared photometry of the micro-quasar gro j1655-40 in quiescence, Astrophys. J. **554**, 1290 (2001).
[124] J. A. Orosz and C. D. Bailyn, Optical observations of GRO J1655-40 in quiescence I: A precise mass for the black hole primary, Astrophys. J. **477**, 876 (1997).
[125] R. Hjellming and M. Rupen, Episodic ejection of relativistic jets by the x-ray transient GRO:J1655-40, Nature (London) **375** (1995) 464.
[126] R. Shafee, J. E. McClintock, R. Narayan, S. W. Davis, L.-X. Li, and R. A. Remillard, Estimating the spin of stellar-mass black holes via spectral fitting of the x-ray continuum, Astrophys. J. Lett. **636**, L113 (2006).
[127] R. C. Reis, A. C. Fabian, R. R. Ross, and J. M. Miller, Determining the spin of two stellar-mass black holes from disc reflection signatures, Mon. Not. R. Astron. Soc. **395**, 1257 (2009).
[128] S. Motta, T. Belloni, L. Stella, T. Muoz-Darias, and R. Fender, Precise mass and spin measurements for a stellar-mass black hole through X-ray timing: The case of GRO J1655-40, Mon. Not. R. Astron. Soc. **437**, 2554 (2014).
[129] J. Greiner, J. Cuby, M. McCaughrean, A. Castro-Tirado, and R. Mennickent, Identification of the donor in the x-ray binary grs $1915+105$, Astron. Astrophys. **373**, L37 (2001).
[130] M. Reid, J. McClintock, J. Steiner, D. Steeghs, R. Remillard, V. Dhawan, and R. Narayan, A parallax distance to the microquasar GRS $1915+105$ and a revised estimate of its black hole mass, Astrophys. J. **796**, 2 (2014).
[131] J. E. McClintock, R. Shafee, R. Narayan, R. A. Remillard, S. W. Davis, and L.-X. Li, The spin of the near-extreme kerr black hole GRS $1915+105$, Astrophys. J. **652**, 518 (2006).
[132] D. Psaltis, D. Perrodin, K. R. Dienes, and I. Mocioiu, Kerr Black Holes are Not Unique to General Relativity, Phys. Rev. Lett. **100**, 091101 (2008).
[133] T. Paul and S. SenGupta, Scalaron tunneling and the fate of antisymmetric tensor fields in $F(R)$ gravity, Classical Quant. Grav. **37**, 225012 (2020).
[134] A. Das, T. Paul, and S. Sengupta, Invisibility of antisymmetric tensor fields in the light of $F(R)$ gravity, Phys. Rev. D **98**, 104002 (2018).
[135] L. Randall and R. Sundrum, A Large Mass Hierarchy from a Small Extra Dimension, Phys. Rev. Lett. **83**, 3370 (1999).

[136] B. Mukhopadhyaya, S. Sen, and S. SenGupta, Bulk torsion fields in theories with large extra dimensions, Phys. Rev. D **65**, 124021 (2002).

[137] B. Mukhopadhyaya, S. Sen, and S. SenGupta, Does a Randall-Sundrum Scenario Create the Illusion of a Torsion Free Universe?, Phys. Rev. Lett. **89**, 121101 (2002); Erratum, Phys. Rev. Lett. **89**, 259902 (2002).

[138] A. Das, B. Mukhopadhyaya, and S. SenGupta, Why has spacetime torsion such negligible effect on the Universe?, Phys. Rev. D **90**, 107901 (2014).

[139] E. Elizalde, S. D. Odintsov, T. Paul, and D. Saez-Chillon Gomez, Inflationary universe in $F(R)$ gravity with antisymmetric tensor fields and their suppression during its evolution, Phys. Rev. D **99**, 063506 (2019).

[140] E. Elizalde, S. D. Odintsov, V. K. Oikonomou, and T. Paul, Logarithmic-corrected R^2 gravity inflation in the presence of Kalb-Ramond fields, J. Cosmol. Astropart. Phys. 02 (2019) 017.

[141] T. Paul and S. SenGupta, Dynamical suppression of spacetime torsion, Eur. Phys. J. C **79**, 591 (2019).

[142] I. Banerjee, B. Mandal, and S. SenGupta, Implications of Einstein-Maxwell dilaton-axion gravity from the black hole continuum spectrum, Mon. Not. R. Astron. Soc. **500**, 481 (2020).

[143] D. MacDonald and K. Thorne, Black-hole electrodynamics—An absolute-space/universal-time formulation, Mon. Not. R. Astron. Soc. **198**, 345 (1982).